The role of H_2O on the extraction of melt from crystallising magmas

Eva Hartung, Gregor Weber, Luca Caricchi

Department of Earth Sciences, University of Geneva, Rue des Maraîchers 13, 1205 Geneva, Switzerland

Corresponding author:

Eva Hartung email: eva.hartung@unige.ch

Keywords: rhyolite-MELTS, silicic volcanism, water content, melt extraction, segregation timescales, Takidani pluton

ABSTRACT

The segregation and accumulation of felsic melts, from crystallising crustal magma reservoirs, is essential for the chemical evolution of the crust and is a phenomenon preceding some of the largest eruptions on Earth. The physical properties of residual melt and magma and the time over which the conditions remain appropriate for melt extraction are important factors controlling the efficiency of melt extraction and the distribution of melt in magma reservoirs. Here we focus on the initial water content (H_2O_i) of magma as it affects both the physical properties of the residual melt and the timescales at which conditions remain appropriate for melt extraction during progressive magma crystallisation. We use rhyolite-MELTS simulations to evaluate the physical evolution of crystallising granodioritic (or dacitic) hydrous magma (i.e. ≥1 wt.% H_2O_i) at shallow depth at 200 MPa. To constrain the solidification timescales of reservoirs containing magmas with initially different water content, we perform 2.5D thermal modelling. We combine these results with calculations of melt extraction velocity by compaction and hindered settling to identify the optimal conditions at which melt segregation occurs. These calculations suggest that hydrous felsic magmas that attain water saturation after 40 wt.% crystallisation (rheological locking point) are best suited for melt extraction. Once water-saturation is achieved, the rate of release of latent heat of crystallisation and with it the time magma spends within a given temperature interval increases while the viscosity of the residual liquid and crystal-liquid density contrast remain favourable for melt segregation. We first test our findings on the Takidani pluton (Japan) because it shows evidence of residual melt segregation from crystallising magma, and is associated with caldera-forming eruptions. We finally generalise our results to crustal magma reservoirs containing hydrous felsic magmas. Our results suggest that if segregation starts at rheological locking (i.e. crystallinity of 40–50 wt.%) upper crustal reservoirs of $\geq$100 km^3 granodioritic (i.e. dacitic) magma with >2 wt.% H_2O_i can produce large melt-rich caps at the top of partially crystallised magma reservoirs in few hundreds to few thousands of years. The formation of separate melt lenses becomes more likely when segregation of melt starts at crystallinities >0.6. Our results suggest that H_2O_i plays an important role in modulating the distribution of eruptible melt in upper crustal reservoirs. Reservoirs of felsic and water-poor magma (<2 wt.% H_2O_i) tend to be associated with the formation of isolated pockets of crystal-poor and eruptible magma, which could account for the often-observed geochemical heterogeneity of the products of large caldera-forming eruptions in the Snake River Plane. The limited dimensions of these eruptible magma pockets make their detection by geophysical methods challenging.

1 Introduction

The accumulation and storage of viscous high-silica melt in shallow magmatic reservoirs is a process preceding some of the largest explosive eruptions on Earth. The distribution of crystal-poor and eruptible lenses of magmas within highly crystallised magma reservoirs cannot be resolved by geophysical methods for intrinsic limits of spatial resolution (Bedrosian et al., 2018; Huang et al., 2015). The timescales of extraction of viscous felsic melt from highly crystallised magma are also only broadly constrained varying from months to thousands of years (Bachmann and Huber, 2018; Druitt et al., 2012; Gualda et al., 2018; Huber et al., 2012; Wilson and Charlier, 2016). Here we use a field example of extraction of felsic melt from crystallising magma in combination with thermal modelling to investigate the role of magma water content on the distribution and timescales of extraction of felsic melts from reservoirs of crystallising felsic magma.

Segregation of interstitial melt from a rheologically-locked partially-crystallised magma body is a potential mechanism for the accumulation of crystal-poor and eruptible rhyolite (Bachmann and Bergantz, 2004; Dufek and Bachmann, 2010; Hildreth, 2004, 1981; Hildreth and Wilson, 2007; Marsh, 1981). Thermo-mechanical simulations suggest that the efficiency of melt extraction for common hydrous silicic magma compositions is highest at crystal contents between 50% and 70% (Dufek and Bachmann, 2010). Moreover, these studies emphasise that the probability of extraction and the amount of interstitial melt segregated is not only controlled by the physical properties of residual melt and magma, but also by the time spent by magma at conditions best suited for melt extraction (Dufek and Bachmann, 2010; Huber et al., 2009). This, in turn, is a function of the ratio between the rate of heat loss and the rate of release of latent heat of crystallisation during progressive cooling and solidification of a magma reservoir, and evolution of the physical properties of the residual melt and magma with increasing crystallinity (Caricchi and Blundy, 2015; Huber et al., 2009; Lee et al., 2015; Melekhova et al., 2013). The results of these studies permit to draw some general conclusions about extraction of residual melt in felsic systems: i) Independently of the process leading to the extraction of residual melt in crystallising felsic magmas, the separation between residual melt and crystals occurs when magma is rheologically locked (i.e. crystal fraction >0.4; Dufek and Bachmann, 2010; Huber et al., 2010; Marsh, 1981); ii) The velocity of residual melt extraction is directly proportional to the ratio between the density difference of crystals and residual melt and the viscosity of the residual melt (Bachmann and Bergantz, 2004; Dufek and Bachmann, 2010); iii) The longer magma spends at conditions suitable for residual melt extraction, the larger is the amount of extracted residual melt (Dufek and Bachmann, 2010; Huber et al., 2009).

Large-scale segregation of rhyolitic melts from highly crystallised magma is commonly inferred to precede the eruption of rhyolitic magma (Bachmann and Bergantz, 2004; Deering et al., 2011; Hildreth and Wilson, 2007), however, evidence for such segregation processes remains scarce or obscure in the intrusive record (Coleman et al., 2004; Gelman et al., 2014; Lee et al., 2015; Vigneresse, 2014). In recent years, various studies have targeted melt extraction processes in the geological record using radiogenic isotopes (Andersen et al., 2017), whole-rock and mineral chemistry (Barnes et al., 2017; Hartung et al., 2017), and rock fabrics (Holness et al., 2017). The Takidani pluton in Central Japan shows evidence of melt segregation processes and is used here as a case study to investigate the formation of bodies of crystal-poor and eruptible melt in the upper crust (Hartung et al., 2017). This pluton has been shown to present the source of dacitic and rhyolitic volcanic eruptions (Harayama, 1992; Kimura and Nagahashi, 2007; Nagahashi et al., 2000). The pluton is texturally zoned, with a gradual transition (over about 50 m) from equigranular granodiorite to porphyritic granite (Fig. 1). Whole rock and mineral chemistry suggest that the porphyritic unit (pGT) was extracted from the underlying granodiorite (GDT) once the residual melt fraction dropped to 40–50 wt.% (Figs. 1, 2a; Hartung et al., 2017). The initial water content of the granodiorite associated with melt segregation is estimated between 3 and 4 wt.% H_2O based on mineral chemistry, crystallisation sequence and relative abundance of mineral phases (Hartung et al., 2017).

In this study, we focus on the effects of the initial water content (H_2O_i) on the timescales magma spends at crystallinities larger than about 40 wt.%, which are considered favourable for the extraction of residual melt (Bachmann and Bergantz, 2004; Dufek and Bachmann, 2010). We first calculate the evolution with temperature and crystallinity of the physical properties of magma and residual melt for granodioritic (i.e. dacitic) magmas with water contents between 1 and 6 wt.%. The velocity of melt extraction for crystallinities between 40 and 80 wt.% are estimated using hindered settling (Davis and Acrivos, 1985) and compaction-driven segregation (McKenzie, 1984). To constrain the maximum timescales available for segregation to occur we perform thermal modelling for reservoirs of different volumes and shapes. The aims of this study are (1) to constrain the effect of H_2O_i on the efficiency of melt extraction, (2) to identify the conditions that led to the extraction of residual melt from the Takidani pluton and estimate the timescales of this process, (3) to define the impact of H_2O_i on the architecture of upper crustal magma reservoirs.

2 Material and methods

2.1 The Takidani Pluton: Evidences for melt segregation

In the following we provide a summary of the main results of a geochemical study previously performed on the Takidani pluton (Hartung et al., 2017), which provides the background and motivation for this study. The Takidani pluton is a well exposed and young pluton (1.6 Ma; Harayama, 1992; Ito et al., 2017), located in the Central Japan Alps. The pluton is vertically exposed over 1800 m (Harayama et al., 2003) from a tectonic contact at the base to a magmatic roof contact with older volcanic rocks (i.e. Hotaka Andesite, Harayama, 1994). Textural, chemical and isotopic evidence of large-scale melt segregation is observed in the upper part of the pluton (Figs. 1, 2; Hartung et al., 2017). The rock textures of the Takidani pluton change from holocrystalline to progressively more porphyritic appearance from the base and centre to the roof of the intrusion. Whole-rock geochemistry shows that the rocks immediately below the porphyritic unit are depleted in incompatible elements, while the porphyritic unit is enriched in incompatible elements (Fig. 1; Hartung et al., 2017). Data obtained through quantitative evaluation of minerals by QEMSCAN and electron microprobe analyses (i.e. EPMA) are used to determine the area percent and chemical composition of the matrix components (equivalent to residual melt composition) throughout the upper section of the Takidani pluton, where evidence for melt extraction is observed (Fig. 1; supplementary data: Table 1). These data show progressive enrichment in the residual melt components defined by quartz (Qtz), alkali feldspar (Kfs) and albite-rich plagioclase ($Plg<An_{30}$) from the equigranular granodiorite (GDT) to the porphyritic granite (pGT; Fig. 1). The relative amounts of quartz, albite (Ab), and orthoclase (Or) and therefore the melt compositions, however, do not change across the textural and chemical transition (Fig. 1; supplementary data: Table 1). This suggests that the residual melt had a

chemical composition close to the granitic minimum after emplacement at approximately 200 MPa (Johannes and Holtz, 1996) and that the extraction of the residual melt, now represented by the porphyritic unit, occurred once magma crystallised sufficiently for the residual melt to acquire a composition close to the granitic minimum (Fig. 1). Mineral chemistry provides additional support for the extraction of residual melt once the magma was rheologically locked (Hartung et al., 2017).

Plagioclase phenocrysts in the granodioritic unit below the porphyritic have cores of different chemistry that are overgrown by a distinct rim of common composition, which is consistent with the composition of plagioclase in the matrix of the porphyritic unit (Hartung et al., 2017). An increase in Rb (incompatible during crystallisation of the Takidani granodiorite; Hartung et al., 2017) in plagioclase phenocrysts increases by more than a factor of two from the core to the common outer rim. This suggest that once magma crystallised to approximately 40–50 wt.%, plagioclase acquired the same composition indicating rheological locking (Fig. 2). Within this crystallinity range the residual melt was extracted leading to the formation of the porphyritic unit of the Takidani pluton that contains matrix plagioclase with the same composition of the plagioclase rims of the underlying granodioritic unit.

Inclusions of orthopyroxene in amphibole, amphibole thermometry, plagioclase composition, and comparison with the phase equilibria experiments of Costa et al. (2004), highlight that amphibole became stable once the magma achieved crystallinities of 40–50 wt.% (Hartung et al., 2017). The late appearance of amphibole at low temperatures and core to rim plagioclase chemistry indicate that the Takidani magma was not initially water-saturated (Costa et al., 2004) and contained initially between 3 and 4 wt.% H_2O.

On the basis of the collected evidence we conclude that the pGT unit represents a lens of residual melt extracted from the underlying GDT granodiorite. The extraction of residual melt from the crystallising magma occurred after the magma became rheologically locked, at which point the residual magma had reached water saturation (Costa et al., 2004; Hartung et al., 2017). The evidence supporting initial water-undersaturation of the magma and melt extraction for the Takidani pluton motivate us to investigate the role of H_2O_i on the extraction of felsic melt from crystallising magmas.

2.2 Rhyolite-MELTS simulations

Existing experimental data do not cover the entire range of temperature and water contents required to trace the evolution of residual melt during cooling and crystallisation of magma in the upper crust (Costa et al., 2004; Holtz et al., 2005; Scaillet and Evans, 1999). Thus, we use rhyolite-MELTS (Gualda et al., 2012) to calculate the chemical and physical evolution of residual melt of dacitic (or granodioritic) magma from liquidus to near solidus temperatures and over the entire range of H_2O_i between 1 wt.% and water saturation. Because granodiorites represent about 95 wt.% of the upper crust (Rudnick and Gao, 2003) with a composition similar to the starting material of Costa et al. (2004), we use the latter for the rhyolite-MELTS calculations. While rhyolite-MELTS it currently not capable of correctly identifying the stability of hydrous phases such as amphibole and biotite, here we use rhyolite-MELTS, especially, to trace the general evolution of residual melt chemistry and magma crystallinity. To test the performance of rhyolite-MELTS we compare the calculated residual melt compositions with residual melts produced experimentally by Costa et al. (2004) using the same starting composition. For all calculations, the confining pressure was fixed at 200 MPa, which are the conditions applied in the experiments of Costa et al. (2004) and comparable to the inferred emplacement depth of many granitic intrusions including the Takidani pluton (Hartung et al., 2017). The oxygen fugacity was initially set to the nickel-nickel oxide buffer (NNO) to calculate the liquidus temperature (for different H_2O_i), but remained unconstrained during progressive heat extraction. The evolution of the residual melt chemistry as function of temperature and H_2O_i calculated with rhyolite-MELTS is comparable to that obtained in the experiments of Costa et al. (2004; Fig. 3). Importantly, rhyolite-MELTS can accurately reproduce the evolution of silica content of the residual melt, which together with water plays a dominating role in controlling the viscosity of silicic melts (Hess and Dingwell, 1996). Additionally, the decrease of melt fraction with temperature for different H_2O_i follows paths that are comparable to those determined experimentally by Whitney (1988; Fig. 4b), hence we consider the rhyolite-MELTS calculations appropriate to compare the evolution of physical properties of hydrous magmas during progressive crystallisation.

To quantify the time magma spends within different temperature intervals we perform isobaric rhyolite-MELTS simulations by removing an equal amount of enthalpy (i.e. 1 J g^{-1}) from the system at each step (n) starting from the liquidus temperature down to a temperature (T) of about 740°C, which corresponds to a residual melt fraction of about 0.1. If a fixed amount of enthalpy is extracted from the magma during solidification, which would be appropriate for quasi-eutectic magma compositions (Gualda et al., 2018), the number of modelling steps within a given temperature interval becomes proportional to the time spent by the magma within a given interval of temperature. This is important to be able to quantify the total time that magma spends within the temperature and crystallinity range at which the conditions are most conducive to melt extraction (Dufek and Bachmann, 2010). Considering that the rate of heat loss will decrease during magma crystallisation because of the decreasing temperature difference between magma and host rocks, our approach increasingly underestimates the time spent within a given temperature range. This is especially the case at intermediate to high crystallinities, where segregation of interstitial melt takes place. The difference between this scenario and one more appropriate for non-eutectic magmas, for which the non-linear rate of heat release over time must be considered, is addressed by thermal modelling.

2.3 Thermal modelling

To provide constrains on the timescales of melt extraction, we use thermal modelling to compute the temporal evolution of temperature in instantaneously emplaced cylindrical magma bodies of various volumes, aspect ratios and initial water contents. We solved the two-dimensional axisymmetric formulation of the heat conduction equation, which can be written as:

$$\rho c \frac{\partial T}{\partial t} = \frac{1}{r}\frac{\partial}{\partial r}\left(rk\frac{\partial T}{\partial r}\right) + \frac{\partial}{\partial z}\left(k\frac{\partial T}{\partial z}\right) + \rho L \frac{\partial X_c}{\partial t} \qquad (1)$$

were T is the temperature, t is the time, r is the radial coordinate relative to the symmetry axis, z is the depth, k is the thermal conductivity, L is the latent heat of crystallisation, ρ is the density, c is the specific heat and X_c is the fraction of crystals in the magma. For a list of the parameters used in the modelling the reader is referred to Table 2 in the supplementary data. The calculations were performed on a numerical grid using an explicit finite difference discretisation of the above equation. The model considers latent heat of crystallisation, which was implemented using our rhyolite-MELTS results to parametrise the crystal fraction (X_c) versus temperature for the different initial water contents used in this study (Fig. 5a). As the dependence of X_c on T is non-linear, the governing equation was solved using an iterative strategy. In all models, we integrated an initial geothermal gradient of 25 °C km^{-1} and a temperature-dependent thermal conductivity (*k*) as described in Whittington et al. (2009) for average crust. The upper (i.e. surface) and lower boundary (i.e. 25–35 km) in the models was set to a fixed temperature determined by the initial geothermal gradient, while zero flux boundary conditions were imposed on the left and right side. Cooling due to circulation of hydrothermal fluids around the magma reservoir was neglected in the modelling and the potential effects of this simplification are discussed in the following.

The setup consists of a 25 x 25 km domain for magma volumes of 100 and 1000 km^3, and a 35 x 35 km domain for intrusions of 10.000 km^3, using 400 x 400 numerical grid for all simulations (supplementary data: Fig. S1). In each model the magma body was intruded instantaneously at 10 km depth at its liquidus temperature and crystallised to near solidus conditions, as determined by the rhyolite-MELTS simulations. To test the effect of reservoir shapes on the solidification history, we ran models with intrusion aspect ratios of 2 and 10 for magma volumes of 100 and 1000 km^3, while model pluton volumes of 10.000 km^3 were only performed with an aspect ratio of 10, due to the large vertical extent of such reservoirs, which makes the application of a single melt fraction-temperature relation unreasonable. Finally, to compare melt segregation velocities to solidification timescales we tracked the temporal propagation of isotherms and melt fraction with depth in the centre of the intrusion.

3 Results

3.1 Thermal, chemical and physical evolution of dacitic magma

Water has an important effect on phase equilibria as it depresses liquidus temperatures and modifies the relationships between temperature, crystallinity, and the physical properties of magma over a wide range of chemical compositions (e.g. viscosity and density of the residual melt; Blatter et al., 2013; Caricchi et al., 2007; Giordano et al., 2008; Hess and Dingwell, 1996; Lange, 1994; Melekhova et al., 2013; Müntener and Ulmer, 2018; Ulmer et al., 2018; Whitney, 1988). Crystallisation of magma leads to a non-linear increase in silica and water content in the residual melt (Fig. 4a-d). Once the residual melt becomes water-saturated, initially water-undersaturated magmas join the *T*-melt fraction trajectory of initially water-saturated magma (Fig. 4b). The non-linear relationships between melt fraction and temperature, contributes to modulate both the timescales magma spends at different temperatures, and the temporal evolution of the physical properties of the residual melt during progressive magma crystallisation. In crystallising magma reservoirs, magma spends relatively more time at temperatures at which the rate of crystallisation (i.e. rate of latent heat release) is highest (Caricchi and Blundy, 2015; Marsh, 1981). Thus, if the crystallisation rate increases once rheological locking is achieved, magma will spend relatively more time at these temperature conditions (Huber, 2009, Caricchi and Blundy, 2015). The time is even larger considering that the rate of heat release from magma reservoirs drops with cooling and progressive decrease of the thermal gradient between magma and host rocks.

Magmas with lower water contents will achieve rheological locking at higher temperatures with respect to water-rich magmas, which will, in turn, impact viscosity, density and velocity of residual melt extraction (Fig. 5b, c; Bachman and Bergantz, 2004). Our calculations show that regardless of H_2O_i of magma, residual melt viscosity increases down to melt fractions of 0.5–0.4 because of decreasing temperature and increasing silica content. At lower melt fractions (<0.4) and once volatile saturation is achieved, the viscosity of the residual melt remains relatively constant independent of H_2O_i (Fig. 5b). Relatively dry melts (H_2O_i ≤2 wt.%) reach a maximum in viscosity before joining the same trajectory of water-richer magmas at lower temperatures

(Fig. 5b). The contrast in density between the solid phase and residual melt spans a wide range of values near liquidus conditions (for different H_2O_i) but becomes less dependent on H_2O_i for melt fractions <0.6 (Fig. 5c). The ratio of the difference in density between crystals and residual melt and the viscosity of the residual melt, which is directly related to the velocity of melt extraction (Bachman and Bergantz, 2004), generally increases with water content (Figs. 5b, c). Based on the physical properties of residual melt and magma, the melt extraction velocity is the fastest for initially water-saturated magmas. However, the total time spent by magma at melt fractions <0.6 (i.e. rheologically locked conditions) is inversely proportional to H_2O_i (Fig. 5d). To assess the relative importance of H_2O_i on the physical properties of magma and the timescales available for melt segregation to occur, we calculate the velocity of melt extraction by hindered settling (Bachmann and Bergantz, 2004) and compaction (McKenzie, 1984) for granodioritic-dacitic magma for melt fraction <0.6. We notice that the formulations used to calculate the velocity of melt extraction are rather simplified, however, such order of magnitude estimates are important to compare the efficiency of residual melt extraction for magmas with different H_2O_i. We do not consider the presence of excess magmatic fluids (i.e. H_2O, CO_2, S) during melt extraction, which can have both positive and detrimental effects on the efficiency of melt extraction (Boudreau, 2016; Caricchi et al., 2018; Parmigiani et al., 2016; Pistone et al., 2015; Sisson and Bacon, 1999).

3.2 Velocities of melt segregation

Hindered settling and compaction-driven segregation describe the relative motion and separation of liquid (i.e. melt) and solid (i.e. crystal) in a two-phase system (i.e. crystallising magma). The process of particle settling in a monodisperse suspension is described by hindered settling

(Equation 2). Compaction-driven segregation defines the process of compacting a porous crystalline mush and resulting melt expulsion (Equation 3). A detailed evaluation of hindered settling and compaction-driven segregation processes is presented in Bachmann and Bergantz (2004) and Lee et al. (2015).

To obtain velocities for hindered settling (U_{hs}) and compaction-driven segregation (V_{comp}) for crystallising dacitic magma we use the physical properties obtained from rhyolite-MELTS simulations. We calculate segregation velocities following the equations provided by Bachmann and Bergantz (2004; and references therein):

$$\boldsymbol{U_{hs} = \frac{2 \cdot r^2 \cdot g \cdot \Delta\varrho}{9 \cdot \mu} \frac{(1-c)^2}{(1+c^{\frac{1}{3}})^{[\frac{5}{3}c(1-c)]}}} \tag{2}$$

$$\boldsymbol{V_{comp} = \frac{\kappa \cdot (1-\phi) \cdot \Delta\varrho \cdot g}{\mu \cdot \phi}} \tag{3}$$

Where r is the crystal radius, g is gravitational acceleration (9.81 ms^{-1}), $\Delta\rho$ is the density difference between crystal and melt, μ is the viscosity, c is the crystal fraction, κ is the permeability and ϕ is the porosity. The permeability is calculated from the porosity, crystal radius and permeability coefficient (K) after McKenzie (1984):

$$\boldsymbol{\kappa = \frac{\phi^3 \cdot r^2}{K(1-\phi)^2}} \tag{4}$$

We consider that porosity is equal to melt fraction and we use K values between 50 and 200 (Bachmann and Bergantz, 2004; Pistone et al. 2015). Here we assume monodisperse suspensions of melt and crystals. As magmas contains crystals of different sizes, and this tends to reduce the permeability with respect to monodisperse systems (Bachmann and Bergantz, 2004; Rust and Cashman, 2011), the volumetric rates of melt extraction calculated here for each grain size are maximum estimates.

To calculate and compare segregation velocities for dacitic magmas with different H_2O_i, we first assume that no convection occurs and that magmas are rheologically locked at crystallinities >40 wt.%. Based on Equation 2, velocities for hindered settling vary between 3.6 and 0.06 m yr^{-1} for water-saturated magmas and melt fractions decreasing from 0.6 to 0.2 (Fig. 6a) using a crystal radius of 3 mm. Velocities for under-saturated magmas are lower (i.e. 1 wt.% H_2O_i; Fig. 6a) and decrease from about 0.22 to 0.02 m yr^{-1} with increasing crystallinity. Segregation velocities for H_2O_i ≥3 wt.% increase in similar fashion as water-saturated melts within the rheologically locked interval (Figs. 5a, 6a). Melt segregation of undersaturated magmas with water content <3 wt.% occurs on timescales up to one magnitude slower as they become water-saturated at lower temperature and at higher crystallinities resulting in slower melt extraction velocities. The timescales of melt extraction processes strongly depend on the crystal size and vary by more than one order of magnitude when considering crystal radii of 1 to 5 mm (Fig. 6b).

We also calculate the velocity of melt extraction considering compaction using a permeability coefficient of 50 and a crystal radius of 3 mm and obtain values between 2.2 m yr^{-1} and 5.0×10^{-4} m yr^{-1} for water-saturated magma and between 1.4×10^{-1} m yr^{-1} and 3.9×10^{-4} m yr^{-1} for water-undersaturated magma. Segregation velocities decrease up to one order of magnitude when applying larger permeability coefficients (i.e. 100–200; Fig. 6d). Velocities of melt extraction for compaction-driven segregation and hindered settling are similar at melt fractions between 0.6 and 0.5, however, compaction velocities decrease more rapidly with decreasing melt fraction than hindered settling (Bachmann and Bergantz, 2004; Lee et al., 2015). Below melt fractions of 0.2, the velocity of compaction driven segregation has been shown to increase relative to hindered settling (Lee et al., 2015). Our results show that residual melt separates most effectively from highly crystallised dacitic magmas if H_2O_i is equal or greater than 3 wt.%, independently of the extraction mechanisms considered (Fig. 6). As phase equilibria and water solubility are both affected by pressure, 3 wt.% H_2O_i is a threshold value appropriate for confining pressures of 200 MPa. The increase of water solubility with pressure could increase the efficiency of melt-extraction at mid to deep crustal levels (i.e. 15–20 km depths), where potentially larger H_2O_i would result in lower melt viscosity and accelerate segregation processes. At such depths, the rate of heat release from magma reservoir is also lower, which would also increase the time available for segregation of residual melt.

3.3 Crystallisation and melt segregation timescales of hydrous felsic magmas

The thermal modelling results allow us to constrain the crystallisation timescales of hydrous dacitic magmas at melt fraction between 0.6 and 0.2, where segregation is most efficient (Dufek and Bachmann, 2010). We track the position of the isotherm corresponding to a given melt fraction along a vertical section through the middle of the intrusion. Each isotherm propagates from the base and the top of the intrusion toward its inner portions (Fig. 7a). We define the "*maximum segregation timescale*" as the time difference between the moment the isotherms corresponding to melt fractions of 0.6 and 0.2 reach the centre of the intrusion (Fig. 7b). The thermal models show that magmas with low H_2O_i (i.e. <3 wt.% H_2O_i) spend substantially more time at rheologically locked conditions than magmas that are initially water-saturated (Fig. 8). For reservoir volumes of 100, 1000, and 10.000 km^3, the maximum timescales for segregation increase from 13 kyr, 61 kyr and 274 kyr for water-saturated magmas to 19 kyr, 84 kyr and 349 kyr, and 20 kyr, 94 kyr and 444 kyr for magmas with H_2O_i of 3 and 2 wt.%, respectively. The timescales available for melt segregation increase by a factor of 4 to 5 with decreasing aspect ratios from 10 to 2 (Fig. 8).

To estimate the maximum melt migration distances, we first calculate the average segregation velocity of hindered settling and compaction (Equations 2, 3) for each melt fraction interval of 0.1 between 0.6 and 0.2. Secondly, each of these values are multiplied by the time required by the corresponding isotherm to reach the core of the intrusion, once the melt fraction within the reservoir has reached 0.6 (Figs. 7a and 9a,b). Because of the relatively high segregation velocities at melt fractions between 0.6 and 0.5, the residual melt can migrate large distances over the duration of isotherm propagation from 0.6 to 0.5 (Figs. 6, 9a,b). For example, maximum segregation distances fall in the order of tens of kilometres for a magma reservoir with a volume of 1000 km^3 (Fig. 9 a,b). The timescales for melt to travel to the roof are fastest for water-saturated magma increasing from 600 to 2500 yr for water-saturated magmas and magmas with H_2O_i of 2 wt.%, respectively (Fig. 9b). These values decrease to about 300 to 1200 yr for reservoir volumes of 100 km^3 and increase to about 1300 and 5400 yr for magma reservoirs with a volume of 10.000 km^3 (Fig. 9b). For a reservoir of 1000 km^3, the time required for the extracted melt to reach the roof by compaction-driven segregation is twice as long and range from 1300 to 5700 yr for water-saturated and magma with 2 wt.% H_2O_i, respectively.

4 Discussion

4.1 *Segregation timescales of the Takidani Pluton*

Magmas of the Takidani Pluton were initially water-undersaturated with water contents of about 3 to 4 wt.% (Hartung et al., 2017; Costa et al., 2004). During crystallisation and melt evolution the residual liquids would have reached volatile saturation at melt fractions between 0.70 (i.e. 4 wt.% H_2O_i) and 0.55 (i.e. 3 wt.% H_2O_i) and temperatures around 820°C to 780°C (Fig. 5a,b). At this point an increase of crystallisation rate and release of latent heat of crystallisation would have resulted in near isothermal crystallisation. A potential indication of this process may come from amphibole thermometry, which suggests the crystallisation of this phase occurred almost entirely in between 800 and 750 °C (Hartung et al., 2017). This could support our hypothesis that magma was thermally buffered over long time periods by the release of latent heat of crystallisation.

Based on our rhyolite-MELTS simulations and thermal modelling we estimate the maximum and minimum timescales over which melt segregation took place in the Takidani Pluton. We consider that the column of melt (*h*) is equal to the thickness of the porphyritic unit (270 m; Fig. 1, Hartung et al. 2017). Velocities of hindered settling segregation of magma with H_2O_i of 3 to 4 wt.% range from 3.1 m yr^{-1} to about 0.06 m yr^{-1} between 0.6 and 0.2 melt fraction for an intermediate crystal radius of 3 mm, which is considered appropriate for granitoids (Bachmann and Bergantz, 2004; Lee et al., 2015) including the Takidani pluton (Fig. 1; Hartung et al., 2017). This would imply that the extraction of the melt producing the porphyritic unit of the Takidani pluton required between about 100 yr and 5000 yr. If we considered a smaller crystal size (i.e. 1 mm) the time required for segregation by hindered settling would increase by approximately one order of magnitude to 1000 yr and 45 kyr. Velocities for compaction-driven segregation for the same water contents and crystal size (i.e. 3 mm) vary between 0.5 m yr^{-1} and 0.0001 m yr^{-1} leading to much slower extraction timescales of about 800 yr to 2 Myr.

The Takidani Pluton has an exposed horizontal extension of about 14 km and exposed vertical extension of about 2 km, which implies a minimum volume of 300 km^3 considering a cylindrical shape. The results of our thermal models show that the time available for segregation in the Takidani Pluton with magmas containing 3 to 4 wt.% H_2O_i varies between 40 and 120 kyr for aspect ratios of 10 and 2, respectively (Fig. 8). The thermal modelling and velocity calculations we performed, show that compaction-driven segregation generally operates at timescales that are larger than estimated solidification timescales and therefore cannot explain the observed segregation in the Takidani Pluton. Hindered settling, on the other side, is a much faster process that can explain the observed melt segregation in the Takidani Pluton. Only in the eventuality that segregation would have started at melt fraction smaller than 0.3, the porphyritic unit of the Takidani pluton would not represent a melt-rich cap near the roof of the pluton. Considering that the base contact of the pluton is tectonic and therefore its volume could be considerably larger than 300 km^3, our results show that sufficient time was available for melt segregation to occur and to form a melt cap via hindered settling (Fig. 10) or processes that operate at similar timescales (i.e. gas filter pressing; Sisson and Bacon, 1999). Finally, evidence from quartz hosted fluid inclusion studies suggest that the Takidani Pluton developed a liquid-dominated hydrothermal systems at some point in the past (Bando et al., 2003; Sekine et al., 2001). Heat advection associated with hydrothermal circulation is not considered in our calculations but would have increased the rate of heat release depending on the vigour of fluid convection (Delaney et al., 1995). This directly decreases the time available for melt segregation (Dutrow et al., 2001), thus increasing the potential for melt to form isolated melt lenses instead of a large cap on top of magmatic reservoirs.

4.2 The control of H_2O_i on the extraction of residual melt from crystallising magmas

Geochemical and petrologic studies show that crystal-poor rhyolites are sourced either from caps at the top of partially crystallised reservoirs (Bachmann and Bergantz, 2004; Hildreth and Wilson, 2007), or from the amalgamation of isolated melt pockets dispersed within a highly crystallised magma body (Wotzlaw et al., 2014, Ellis et al., 2014). The processes responsible for the generation of reservoirs with such distinct architecture are not yet fully understood. The total distance over which melt migrates before the system cools to its solidus temperature, controls the final distribution of crystal-poor felsic melt in magmatic reservoirs. Thus, the maximum amount of rhyolitic melt that can potentially be accumulated depends on H_2O_i and the temperature of the magma, the volume and shape of the magma body and the temperature difference of the intruding magma and the host rock (i.e. thermal gradient). We have illustrated that the initial amount of water dissolved in magmas affects (1) the physical properties and segregation velocities of residual melts (Figs. 5, 6) and (2) the total amount of time spent within the rheologically locked temperature interval (Figs. 7, 8; Caricchi and Blundy, 2015).

Our calculations show that crystal size is an important factor controlling segregation velocities of residual melt (i.e. Bachmann and Bergantz, 2004), while the initial water content affect both the melt extraction velocity and the release of latent heat, which, in turn, modulates the time spent by the magma within different temperature intervals. Volume and shape of the magma reservoir affect the thermal evolution and timescales of reservoir solidification. In case of hindered settling, residual melts of magmas that contain at least 2 wt.% H_2O_i are extracted sufficiently fast to form melt rich caps at or near the roof of the magma reservoir (Fig. 8) considering an intermediate crystal size of 3 mm. Magma reservoirs that have a minimum volume of 1000 km^3 can facilitate complete melt segregation for smaller crystal sizes (Fig. 10a). On the other hand, smaller magma bodies (i.e. 100 km^3) with less than 2 wt.% H_2O_i are less likely to form any melt-rich body. Although magmas with 1 wt.% H_2O_i spent half of their solidification time within the rheological locking temperature window (Fig. 5d), the high viscosity of the residual melt (i.e. low segregation velocity) does not favour the formation of caps or melt-rich lenses of crystal-poor rhyolite under the modelled conditions. The boundaries between caps and lenses, thus, may largely depend on the segregation velocity of the residual melt. Slower segregation of the residual melt, for instance through compaction or through hindered settling with smaller crystals (<3 mm radius; Bachmann and Bergantz, 2004), will decrease the probability of forming caps of crystal-poor rhyolitic melt and increase the probability of forming isolated melt-rich lenses. The onset of melt segregation processes can play an important role in the formation of crystal-poor rhyolite (Figs. 9, 10). The likelihood of forming a crystal-poor cap is very high when segregation processes start early within the rheologically locked crystallinity window, and segregation velocities remain elevated (Figs. 6a, 10). Unless magmas are extremely dry (1 wt.% H_2O_i), H_2O_i of magma does not seem to play a major role in controlling the architecture of the reservoir and melt distribution when melt extraction occurs at high melt fractions (i.e. 0.6; Fig. 9a,b). The timescales of melt accumulation, however, are strongly dependent on the type of segregation process (i.e. hindered settling and compaction) and on H_2O_i: melts containing higher amounts of water migrate faster (Fig. 9a,b) because of their lower viscosities (Fig. 5b). When the onset of melt segregation occurs at relatively low melt fractions (i.e. 0.3), H_2O_i may influence whether caps or separate lenses are formed. Water-undersaturated magmas may have a higher chance to form melt caps compared to magmas with higher water contents, because of their prolonged cooling timescales at rheologically locked conditions (Fig. 10c). Overall, at low melt fraction timescales for melt segregation are short, which together with low melt segregation velocities decreases the capacity of these magmas to form thick melt-rich bodies near the roof of the reservoir and the formation of isolated melt-rich lenses becomes more likely.

5 Conclusions

The interplay between magma water content, the viscosity of residual melt, the density contrast between residual melt and crystals, and the time spent within the rheologically locked crystallinity interval, favoured the extraction of residual melt from the Takidani pluton (Fig. 5). Our time estimates for melt segregation indicate that the extraction of residual liquids in silicic reservoirs like the Takidani Pluton occurs over centuries and millennia which is consistent with other studies (Bachmann and Huber, 2018).

While H_2O_i of magma has a significant control on the segregation timescales of magmatic reservoirs, the architecture of magmatic reservoirs is controlled by the magma crystallinity, crystal size and permeability at the onset of melt segregation processes. The results from our models suggest that hydrous felsic magma are prone to form large melt caps at the roof of a magma reservoir if segregation occurs early at intermediate melt fractions (e.g. 0.6–0.5). However, if segregation starts at low melt fractions (i.e. compaction-driven segregation), silica-rich melts may not be able to reach the roof of magma reservoirs because of their low segregation velocity and may form isolated melt lenses within highly crystallised magma. A similar reservoir configuration is likely for water-poor magma, as residual melt segregation require longer timescales (Fig. 7). The drainage of isolated crystal-poor lenses of magma during eruption may account for the chemically heterogeneous nature of rhyolitic eruptions in relatively dry systems such as Yellowstone (Ellis et al., 2014; Wotzlaw et al., 2014). We notice that our study focuses on felsic magmas characteristic of some of the large eruptions on Earth; the dependency of viscosity and density of magma and residual melt on chemistry does not warrant the extension of our conclusions to systems of significantly different chemistry.

The timescales of melt segregation vary by several orders depending on the crystal size and the mechanism that dominates the extraction process (Fig. 6b). The extremely short timescales obtained from geochronology and geospeedometry (months to decades; Druitt et al., 2012; Gualda et al., 2018; Wilson and Charlier, 2016), are difficult to explain by gravity-driven segregation even considering a larger crystal size (>5 mm).

Despite limitations, our calculations provide a framework to deduce some of the additional factors that may influence the capacity of magmatic systems to contain lenses or caps of eruptible felsic melt. For example, large systems such as Yellowstone host well-developed hydrothermal systems, which increases the rate of heat extraction from magmatic systems with respect to what we consider here. This directly decreases the time available for melt segregation (Dutrow et al., 2001), thus increasing the potential for melt to form isolated melt lenses instead of large caps on top of magmatic reservoirs. Ultimately the complex feedbacks between magma chemistry and its physical properties and the thermal evolution of magmatic systems require a multidisciplinary approach (Gualda et al., 2018; Holness, 2018; Huber and Parmigiani, 2018) to identify the potential signs of an impending volcanic eruption. Our results suggest that for hydrous felsic magmatic systems H_2O_i of magma plays an important role on the extraction of residual melt by affecting both the evolution of the physical properties of magma with temperature and the time magma spends within different temperature intervals.

6 Acknowledgements

We are grateful to Guilherme Gualda and an anonymous reviewer for their detailed and constructive feedback, which has significantly improved this article. We would also like to thank the editor Tamsin Mather for handling this contribution and additional insightful comments. This project was supported by the Swiss National Science Foundation [SNSF grant 200021_150204, 200020_172702]. EH was also financially supported by the Japan Society for the Promotion of

Science (GR17103). LC and GW received additional funding from the European Research Council (ERC) under the European Union’s Horizon 2020 research and innovation program (grant agreement 677493-FEVER).

7 References

Andersen, N.L., Singer, B.S., Jicha, B.R., Beard, B.L., Johnson, C.M., Licciardi, J.M., 2017. Pleistocene to holocene growth of a large upper crustal rhyolitic magma reservoir beneath the active laguna del Maule Volcanic Field, Central Chile. J. Petrol. 58, 85–114. https://doi.org/10.1093/petrology/egx006

Bachmann, O., Bergantz, G., 2004. On the Origin of Crystal-poor Rhyolites : Extracted from Batholithic Crystal Mushes. J. Petrol. 45, 1565–1582. https://doi.org/10.1093/petrology/egh019

Bachmann, O., Huber, C., 2018. The inner workings of crustal distillation columns; the physical mechanisms and rates controlling phase separation in silicic magma reservoirs. J. Petrol. egy103. https://doi.org/10.1093/petrology/egy103

Bando, M., Bignall, G., Sekine, K., Tsuchiya, N., 2003. Petrography and uplift history of the Quaternary Takidani Granodiorite : could it have hosted a supercritical (HDR) geothermal reservoir? J. Volcanol. Geotherm. Res. 120, 215–234.

Barnes, C.G., Berry, R., Barnes, M.A., Ernst, W.G., 2017. Trace element zoning in hornblende: Tracking and modeling the crystallization of a calc-alkaline arc pluton. Am. Mineral. 102, 2390–2405. https://doi.org/10.2138/am-2017-6063

Bedrosian, P.A., Peacock, J.R., Bowles-Martinez, E., Schultz, A., Hill, G.J., 2018. Crustal inheritance and a top-down control on arc magmatism at Mount St Helens. Nat. Geosci. 11, 865–870. https://doi.org/10.1038/s41561-018-0217-2

Blatter, D.L., Sisson, T.W., Hankins, W. Ben, 2013. Crystallization of oxidized, moderately hydrous arc basalt at mid- to lower-crustal pressures: Implications for andesite genesis. Contrib. to Mineral. Petrol. 166, 861–886. https://doi.org/10.1007/s00410-013-0920-3

Boudreau, A., 2016. Bubble migration in a compacting crystal-liquid mush. Contrib. to Mineral. Petrol. 171, 32. https://doi.org/10.1007/s00410-016-1237-9

Caricchi, L., Blundy, J., 2015. Experimental petrology of monotonous intermediate magmas. Geol. Soc. London, Spec. Publ. 422, 105–130. https://doi.org/10.1144/SP422.9

Caricchi, L., Burlini, L., Ulmer, P., Gerya, T., Vassalli, M., Papale, P., 2007. Non-Newtonian rheology of crystal-bearing magmas and implications for magma ascent dynamics. Earth Planet. Sci. Lett. 264, 402–419. https://doi.org/10.1016/j.epsl.2007.09.032

Caricchi, L., Sheldrake, T.E., Blundy, J., 2018. Modulation of magmatic processes by CO2flushing. Earth Planet. Sci. Lett. 491, 160–171. https://doi.org/10.1016/j.epsl.2018.03.042

Coleman, D.S., Gray, W., Glazner, A.F., 2004. Rethinking the emplacement and evolution of zoned plutons: Geochronologic evidence for incremental assembly of the Tuolumne Intrusive Suite, California. Geology 32, 433–436. https://doi.org/10.1130/G20220.1

Costa, F., Scaillet, B., Pichavant, M., 2004. Petrological and Experimental Constraints on the Pre-eruption Conditions of Holocene Dacite from Volcan San Pedro (36°S, Chilean Andes) and the Importance of Sulphur in Silicic Subduction-related Magmas. J. Petrol. 45, 855–881. https://doi.org/10.1093/petrology/egg114

Davis, R.H., Acrivos, A., 1985. Sedimentation of Noncolloidal Particles at Low Reynolds Numbers. Annu. Rev. Fluid Mech. 17, 91–118.

https://doi.org/10.1146/annurev.fl.17.010185.000515

Deering, C.D., Cole, J.W., Vogel, T.A., 2011. Extraction of crystal-poor rhyolite from a hornblende-bearing intermediate mush: A case study of the caldera-forming Matahina eruption, Okataina volcanic complex. Contrib. to Mineral. Petrol. 161. https://doi.org/10.1007/s00410-010-0524-0

Delaney, P.T., Sass, J.H., Duffield, W.A., Kauahikaua, J.P., 1995. Temperature and response time of magma hydrothermal systems, with an example from Kilauea, Hawaii. [Proceedings] 1239–1244.

Druitt, T.H., Costa, F., Deloule, E., Dungan, M., Scaillet, B., 2012. Decadal to monthly timescales of magma transfer and reservoir growth at a caldera volcano. Nature 482, 77–80. https://doi.org/10.1038/nature10706

Dufek, J., Bachmann, O., 2010. Quantum magmatism: Magmatic compositional gaps generated by melt-crystal dynamics. Geology 38, 687–690. https://doi.org/10.1130/G30831.1

Dutrow, B.L., Travis, B.J., Gable, C.W., Henry, D.J., 2001. Coupled heat and silica transport associated with dike intrusion into sedimentary rock: effects on isotherm location and permeability evolution. Geochim. Cosmochim. Acta 65, 3749–3767. https://doi.org/https://doi.org/10.1016/S0016-7037(01)00704-9

Ellis, B.S., Bachmann, O., Wolff, J. a., 2014. Cumulate fragments in silicic ignimbrites: The case of the Snake River Plain. Geology 42, 431–434. https://doi.org/10.1130/G35399.1

Gelman, S.E., Deering, C.D., Bachmann, O., Huber, C., Gutiérrez, F.J., 2014. Identifying the crystal graveyards remaining after large silicic eruptions. Earth Planet. Sci. Lett. 403, 299–306. https://doi.org/10.1016/j.epsl.2014.07.005

Giordano, D., Russell, J.K., Dingwell, D.B., 2008. Viscosity of magmatic liquids: A model.

Earth Planet. Sci. Lett. 271, 123–134. https://doi.org/10.1016/j.epsl.2008.03.038

Gualda, G.A.R., Ghiorso, M.S., Lemons, R. V., Carley, T.L., 2012. Rhyolite-MELTS: a Modified Calibration of MELTS Optimized for Silica-rich, Fluid-bearing Magmatic Systems. J. Petrol. 53, 875–890. https://doi.org/10.1093/petrology/egr080

Gualda, G.A.R., Gravley, D.M., Conner, M., Hollmann, B., Pamukcu, A.S., Bégué, F., Ghiorso, M.S., Deering, C.D., 2018. Climbing the crustal ladder: Magma storage-depth evolution during a volcanic flare-up. Nat. Commun. 1–10. https://doi.org/10.1093/gji/ggw416

Harayama, S., 1994. Cooling History of the youngest exposed pluton in the World - The Plio-Pleistocene Takidani Granodiorite (Japan Alps, central Japan). Mem. Geol. Soc. Japan 43, 87–97.

Harayama, S., 1992. Geology Youngest exposed granitoid pluton on Earth : Cooling and rapid uplift of the Pliocene-Quaternary Takidani Granidiorite in the Japan Alps, central Japan. Geology 20, 657–660. https://doi.org/10.1130/0091-7613(1992)020<0657

Harayama, S., Wada, H., Yamaguchi, Y., 2003. Trip A1 Quaternary and Pliocene granites in the Northern Japan Alps. Hutt. Symp. V, F. Guideb.

Hartung, E., Caricchi, L., Floess, D., Wallis, S., Harayama, S., Kouzmanov, K., Chiaradia, M., 2017. Evidence for residual melt extraction in the Takidani Pluton, Central Japan. J. Petrol. 58, 763–788. https://doi.org/10.1093/petrology/egx033

Hess, K.-U., Dingwell, D.D., 1996. Viscosities of hydrous leucogranitic melts: A non-Arrhenian model. Am. Mineral. 81, 1297–1300. https://doi.org/10.2138/AM-1996-9-1031

Hess, K.U., Dingwell, D.B., 1996. Viscosities of hydrous leucogranitic melts : A non-Arrhenian on the nature and efficiency of magmatic processes . As pendence (H20 concentration in weight percent) for each. Am. Mineral. 81, 1297–1300. https://doi.org/10.1016/0016-

7037(82)90381-7

Hildreth, W., 2004. Volcanological perspectives on Long Valley , Mammoth Mountain , and Mono Craters : several contiguous but discrete systems. J. Volcanol. Geotherm. Res. 136, 169–198. https://doi.org/10.1016/j.jvolgeores.2004.05.019

Hildreth, W., 1981. Gradients in silicic magma chambers: Implications for lithospheric magmatism. J. Geophys. Res. Solid Earth 86, 10153–10192. https://doi.org/10.1029/JB086iB11p10153

Hildreth, W., Wilson, C.J.N., 2007. Compositional Zoning of the Bishop Tuff. J. Petrol. 48, 951–999. https://doi.org/10.1093/petrology/egm007

Holness, M.B., 2018. Melt segregation from silicic crystal mushes: a critical appraisal of possible mechanisms and their microstructural record. Contrib. to Mineral. Petrol. 173, 1–17. https://doi.org/10.1007/s00410-018-1465-2

Holness, M.B., Vukmanovic, Z., Mariani, E., 2017. Assessing the role of compaction in the formation of adcumulates: A microstructural perspective. J. Petrol. 58, 643–674. https://doi.org/10.1093/petrology/egx037

Holtz, F., Sato, H., Lewis, J., Behrens, H., Nakada, S., 2005. Experimental petrology of the 1991-1995 Unzen dacite, Japan. Part I: Phase relations, phase composition and pre-eruptive conditions. J. Petrol. 46, 319–337. https://doi.org/10.1093/petrology/egh077

Huang, H.-H., Lin, F.-C., Schmandt, B., Farrell, J., Smith, R.B., Tsai, V.C., 2015. The Yellowstone magmatic system from the mantle plume to the upper crust. Science (80-.). 348, 773 LP-776.

Huber, C., Bachmann, O., Dufek, J., 2012. Crystal-poor versus crystal-rich ignimbrites : A competition between stirring and reactivation. Society 1–4.

https://doi.org/10.1130/G32425.1

Huber, C., Bachmann, O., Dufek, J., 2010. The limitations of melting on the reactivation of silicic mushes. J. Volcanol. Geotherm. Res. 195, 97–105. https://doi.org/10.1016/j.jvolgeores.2010.06.006

Huber, C., Bachmann, O., Manga, M., 2009. Homogenization processes in silicic magma chambers by stirring and mushification (latent heat buffering). Earth Planet. Sci. Lett. 283, 38–47. https://doi.org/10.1016/j.epsl.2009.03.029

Huber, C., Parmigiani, A., 2018. A Physical Model for Three-Phase Compaction in Silicic Magma Reservoirs. J. Geophys. Res. Solid Earth 2685–2705. https://doi.org/10.1002/2017JB015224

Ito, H., Spencer, C.J., Danišík, M., Hoiland, C.W., 2017. Magmatic tempo of Earth's youngest exposed plutons as revealed by detrital zircon U-Pb geochronology. Sci. Rep. 7, 12457. https://doi.org/10.1038/s41598-017-12790-w

Johannes, W., Holtz, F., 1996. Petrogenesis and Experimental Petrology of Granitic Rocks. Springer-Verlag, Berlin, Heidelberg, New York.

Kimura, J.-I., Nagahashi, Y., 2007. Origin of a voluminous iron-enriched high-K rhyolite magma erupted in the North Japan Alps at 1.75 Ma: Evidence for upper crustal melting. J. Volcanol. Geotherm. Res. 167, 81–99. https://doi.org/10.1016/j.jvolgeores.2007.02.004

Lange, R.A., 1994. The Effects of H2O, CO2 and F on the Density and Viscosity of Silicate Melts. Rev. Mineral. Geochemistry 30, 331–370.

Lee, C.-T.A., Morton, D.M., Farner, M.J., Moitra, P., 2015. Field and model constraints on silicic melt segregation by compaction/hindered settling: The role of water and its effect on latent heat release. Am. Mineral. 100, 1762–1777.

Marsh, B.D., 1981. On the crystallinity, probability of occurrence, and rheology of lava and magma. Contrib. to Mineral. Petrol. 78, 85–98. https://doi.org/10.1007/BF00371146

McKenzie, D., 1984. The generation and compactation of partially molten rock. J. Petrol. 25, 713–765.

Melekhova, E., Annen, C., Blundy, J., 2013. Compositional gaps in igneous rock suites controlled by magma system heat and water content. Nat. Geosci. 6, 385–390. https://doi.org/10.1038/ngeo1781

Müntener, O., Ulmer, P., 2018. Arc crust formation and differentiation constrained by experimental petrology. Am. J. Sci. 318, 64–89. https://doi.org/10.2475/01.2018.04

Nagahashi, Y., Satoguchi, Y., Yoshikawa, S., 2000. Correlation and stratigraphic eruption age of the pyroclastic flow deposits and wide spread volcanic ashes intercalated in the Pliocene-Pleistocene strata, central Japan. J. Geol. Soc. Japan 106, 51–69.

Parmigiani, A., Faroughi, S., Huber, C., Bachmann, O., Su, Y., 2016. Bubble accumulation and its role in the evolution of magma reservoirs in the upper crust. Nature 532, 492–495. https://doi.org/10.1038/nature17401

Pistone, M., Arzilli, F., Dobson, K.J., Cordonnier, B., Reusser, E., Ulmer, P., Marone, F., Whittington, A.G., Mancini, L., Fife, J.L., Blundy, J.D., 2015. Gas-driven filter pressing in magmas: Insights into in-situ melt segregation from crystal mushes. Geology 43, G36766.1. https://doi.org/10.1130/G36766.1

Rudnick, R.L., Gao, S., 2003. Composition of the Continental Crust, in: Treatise on Geochemistry. Elsevier, pp. 1–64. https://doi.org/10.1016/B0-08-043751-6/03016-4

Rust, A.C., Cashman, K. V., 2011. Permeability controls on expansion and size distributions of pyroclasts. J. Geophys. Res. Solid Earth 116, 1–17. https://doi.org/10.1029/2011JB008494

Scaillet, B., Evans, B.W., 1999. The 15 June 1991 Eruption of Mount Pinatubo . I . Phase Equilibria and Pre-eruption P–T–fO2–fH2O Conditions of the Dacite Magma. J. Petrol. 40, 381–411.

Sekine, K., Bignall, G., Tsuchiya, N., Nakatsuka, K., 2001. Evidence for Fluid Flow in Non-Brittle Takidani Granite Implications for Utilization of DSGRs. Geotherm. Resour. Counc. Trans. 25, 243–248.

Sisson, T.W., Bacon, C.R., 1999. Gas-driven filter pressing in magmas. Geology 27, 613–616. https://doi.org/10.1130/0091-7613(1999)027<0613

Ulmer, P., Kaegi, R., Müntener, O., 2018. Experimentally derived intermediate to silica-rich arc magmas by fractional and equilibrium crystallization at 1·0 GPa: An evaluation of phase relationships, compositions, liquid lines of descent and oxygen fugacity. J. Petrol. 59, 11–58. https://doi.org/10.1093/petrology/egy017

Vigneresse, J.-L., 2014. Textures and melt-crystal-gas interactions in granites. Geosci. Front. https://doi.org/10.1016/j.gsf.2014.12.004

Whitney, J.A., 1988. The origin of granite: The role and source of water in the evolution of granitic magmas. Geol. Soc. Am. Bull. 100, 1886–1897.

Whittington, A.G., Hofmeister, A.M., Nabelek, P.I., 2009. Temperature-dependent thermal diffusivity of the Earth’s crust and implications for magmatism. Nature 458, 319–21. https://doi.org/10.1038/nature07818

Wilson, C.J.N., Charlier, B.L.A., 2016. The life and times of silicic volcanic systems. Elements 12, 103–108. https://doi.org/10.2113/gselements.12.2.103

Wotzlaw, J.-F., Bindeman, I.N., Watts, K.E., Schmitt, A.K., Caricchi, L., Schaltegger, U., 2014. Linking rapid magma reservoir assembly and eruption trigger mechanisms at evolved

Yellowstone-type supervolcanoes. Geology 42, 807–810. https://doi.org/10.1130/G35979.1

FIGURE CAPTIONS

Figure 1:

Evidence for melt segregation in the upper section of the Takidani Pluton. (left) QEMSCAN images collected from the granodiorite (1; GDT) to the porphyritic portion of the pluton (5; pGT). (top right) Variations of Rb and Sr whole-rock content from GDT to pGT. (bottom right) Interstitial residual melt variations represented by quartz (pink), orthoclase (green) and plagioclase with anorthite content <30 wt.% (orange). The fraction of interstitial residual melt (x_{melt}), gradually increases from the GDT unit towards the pGT unit. The content of quartz, orthoclase and albite, normalised to a fraction of 1, remain relative constant and suggest that the residual melt composition was buffered at the granitic minimum (Johannes and Holtz, 1996).

Figure 2:

Chemical variability in whole rock (a) and mineral chemistry (b). (a) Assimilation and fractional crystallisation (AFC) models (Hartung et al., 2017) performed on whole rock analyses show that compositional diversity is dominantly produced by crystal fractionation. The grey dashed lines and numbers on the side show the amount of melt (i.e. 60 wt.%) and assimilation (i.e. 3.2 wt.%). The evolution of Rb concentration as function of $^{86}Sr/^{87}Sr$ is calculated for different bulk partition coefficients (D_{Rb}). (b) Concentrations of Rb in plagioclase phenocrysts (i.e. sample EH70) increase from 0.54 to 1.31 ppm from core to rim, respectively, and point towards a progressive enrichment of the incompatible element Rb in the melt phase through crystal fractionation. The grey dashed lines and number below indicate the amount of melt fraction.

Figure 3:

Comparison between rhyolite-MELTS simulations (lines) and the matrix glass compositions (circles) measured between 950°C and 800°C by Costa et al. (2004). The colour contouring indicates the initial water content (H_2O_i) of the starting material (Costa et al. 2004). Rhyolite-MELTS simulations and experiments are in broad agreement and show the effect of H_2O_i on the chemical evolution (i.e. SiO_2, Al_2O_3, Na_2O, K_2O) of residual melt with decreasing temperature. No experimental data is available below 800°C.

Figure 4:

Results of rhyolite-MELTS simulations for dacitic magma with composition similar to the Takidani granodiorite and the starting material of Costa et al. (2004). (a) Evolution of the water content of residual melts as function of temperature. (b) Relationship between water content of the residual melt and melt fraction. (c) Silica content of the residual melt versus temperature. (d) Water content versus silica content of the residual melt.

Figure 5:

Physical melt fraction and physical properties of residual melt and magma calculated with rhyolite-MELTS. (a) Relationship between melt fraction and temperature. (b) Evolution of melt viscosity (logarithmic) as function of melt fraction. (c) Density difference between crystals and the residual melt as function of melt fraction. (d) Fraction of the total time spent by the magma within each interval of melt fraction. This is calculated by normalising the number of simulation step within a melt fraction unit of 0.02 to the total amount of steps between 1.0 and 0.1 melt fraction assuming constant heat loss.

Figure 6:

Velocities of melt segregation as function of the melt fraction for magma with different H_2O_i for hindered settling (a, b) and compaction-driven segregation (c, d). (a) Hindered settling velocity for different H_2O_i and crystal radius of 3 mm. (b) Hindered settling velocity for water-saturated magma containing crystals of different radii (r). (c) Velocity of compaction-driven segregation for different H_2O_i and magma with crystal of 3 mm radius. (d) Compaction-driven segregation velocity for water-saturated magma, calculated for different permeability coefficients (K) and crystal radius of 3 mm. Segregation velocities are calculated using the physical properties obtained from rhyolite-MELTS simulations.

Figure 7:

(a) Vertical position of the isotherms, corresponding to different melt fractions (Mf), along a vertical section through the centre of the intrusion as function of time. Reservoir thickness of 0 m presents the top. Location of isotherms are shown for a dacitic magma with H_2O_i of 2 wt.%. (b) Maximum segregation timescales for magma reservoirs with different H_2O_i. Isotherm curves are shown for a magma reservoir of 1000 km^3 with an aspect ratio (AR) of 10. The maximum segregation timescales increase with decreasing H_2O_i of magma.

Figure 8:

Maximum timescales available for segregation for different reservoir volumes, H_2O_i and aspect ratios of the magma reservoir. Curves were obtained by fitting the thermal modelling results using 2nd and 3rd order polynomials (supplementary data: Table 3).

Figure 9:

(a, b) Maximum segregation distance for a reservoir volume of 1000 km^3 and aspect ratio of 10 based on hindered settling and compaction velocities corresponding to an intermediate crystal radius (i.e. r = 3 mm). (c, d) Time required by the residual melt (extracted by hindered settling and compaction) to reach the roof of the magma reservoir for reservoirs of 100, 1000 and 10.000 km^3. The y-axis presents the onset of melt segregation for intervals of 0.1 starting at 0.6, 0.5, 0.4 and 0.3.

Figure 10:

Schematic model for the formation of melt caps and melt pockets for different volumes and H_2O_i for hindered settling. (a) Full segregation is expected in reservoir >100 km^3 for crystal radii >1 mm for the case that segregation processes start at melt fraction of 0.5 or higher. (b) When melt segregation starts at Mf<0.4 only reservoirs that are larger than 100 km^3 or that have low H_2O_i are expected to form melt caps. (c) Partial melt segregation and the formation of crystal lenses are most likely to occur if segregation occurs at high crystallinity. Solidification of the reservoir without significant segregation is expected for magmas with H_2O_i <<2 wt.%. The Takidani Pluton most likely formed a coherent melt cap that may have been erupted.

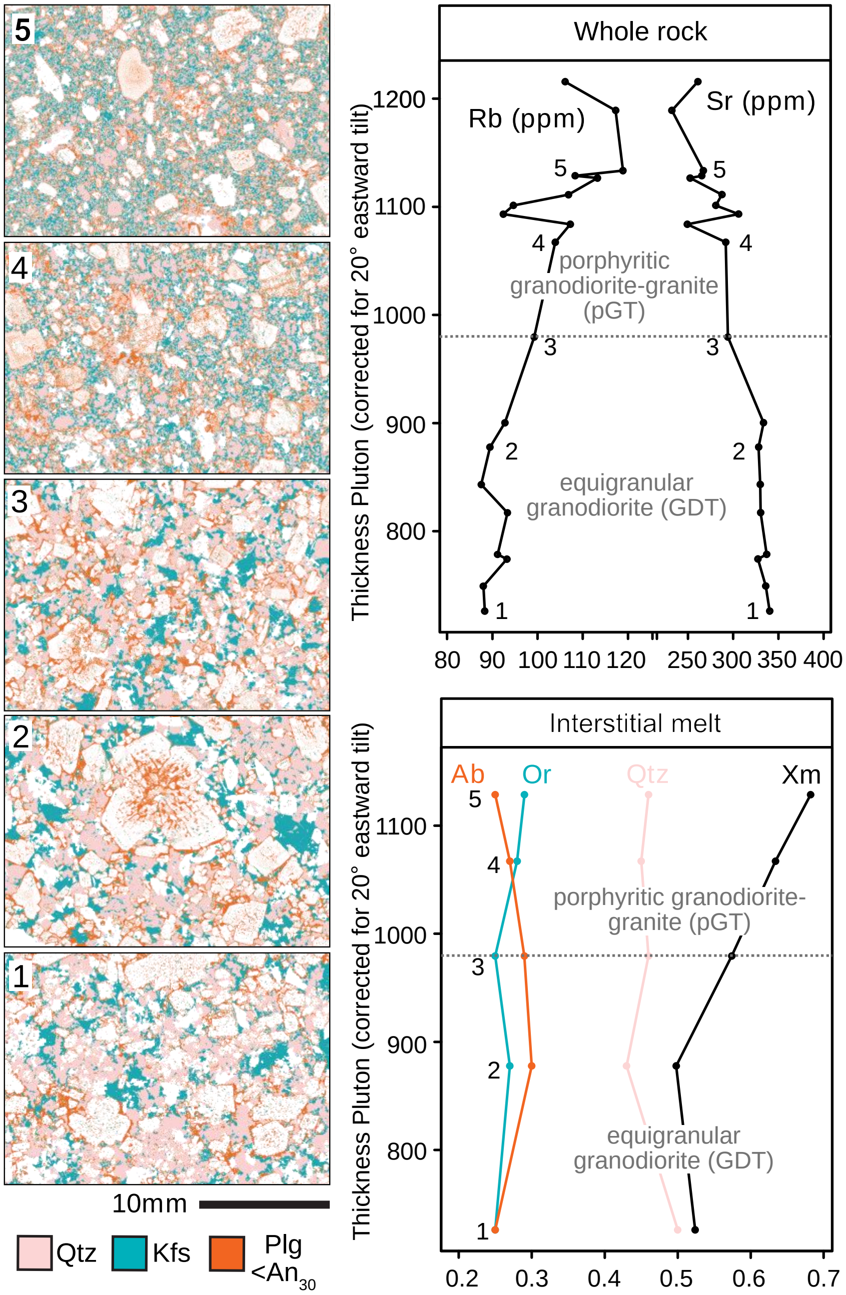

5
4
3
2
1
10mm
Qtz
Kfs
Plg <An$_{30}$
Whole rock
Rb (ppm)
Sr (ppm)
Thickness Pluton (corrected for 20° eastward tilt)
1200
1100
1000
900
800
porphyritic granodiorite-granite (pGT)
equigranular granodiorite (GDT)
80
90
100
110
120
250
300
350
400
Interstitial melt
Ab
Or
Qtz
Xm
0.2
0.3
0.4
0.5
0.6
0.7

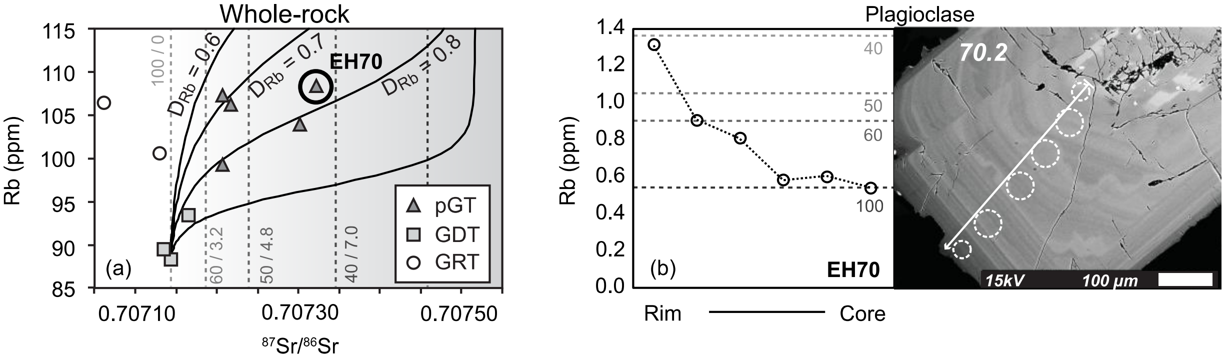
Whole-rock
Rb (ppm)
115
110
105
100
95
90
85
0.70710
0.70730
0.70750
^{87}Sr/^{86}Sr
100 / 0
60 / 3.2
50 / 4.8
40 / 7.0
D_{Rb} = 0.6
D_{Rb} = 0.7
D_{Rb} = 0.8
EH70
▲ pGT
■ GDT
○ GRT
(a)
Plagioclase
Rb (ppm)
1.4
1.2
1.0
0.8
0.6
0.4
0.2
0.0
40
50
60
100
(b)
EH70
Rim
Core
70.2
15kV
100 µm

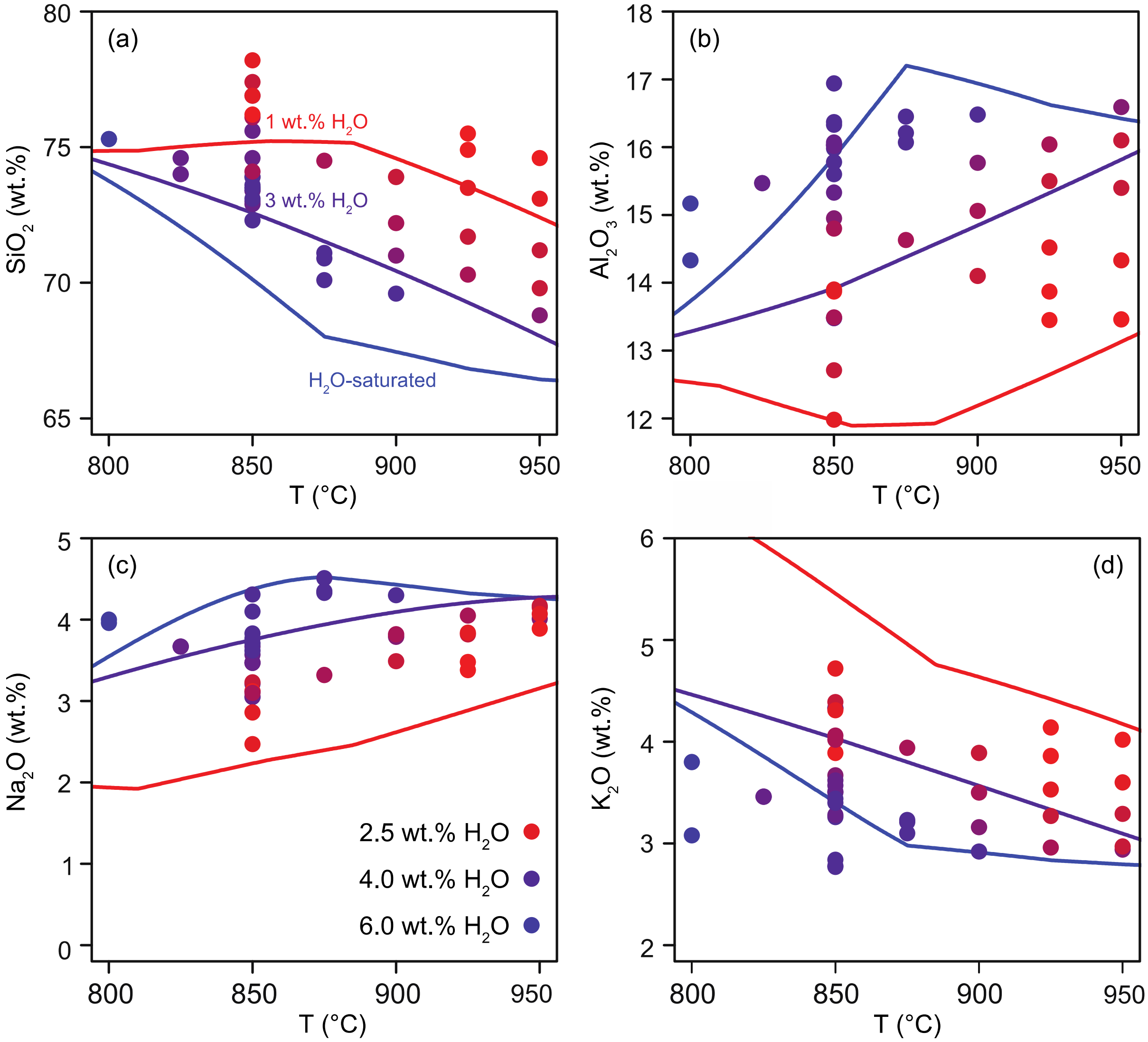
(a)
SiO$_2$ (wt.%)
80
75
70
65
1 wt.% H$_2$O
3 wt.% H$_2$O
H$_2$O-saturated
800
850
900
950
T (°C)
(b)
Al$_2$O$_3$ (wt.%)
18
17
16
15
14
13
12
800
850
900
950
T (°C)
(c)
Na$_2$O (wt.%)
5
4
3
2
1
0
2.5 wt.% H$_2$O
4.0 wt.% H$_2$O
6.0 wt.% H$_2$O
800
850
900
950
T (°C)
(d)
K$_2$O (wt.%)
6
5
4
3
2
800
850
900
950
T (°C)

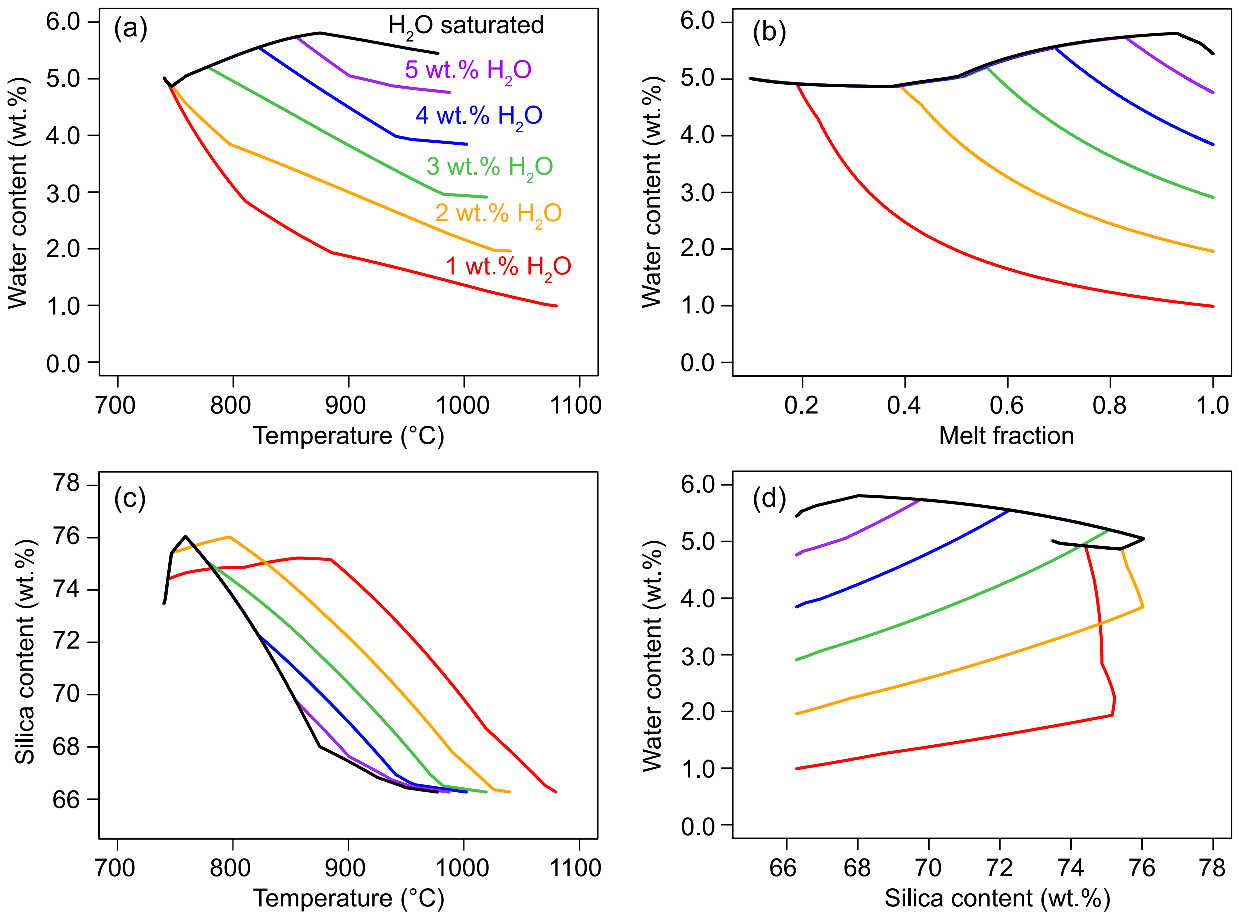
(a)
H$_2$O saturated
5 wt.% H$_2$O
4 wt.% H$_2$O
3 wt.% H$_2$O
2 wt.% H$_2$O
1 wt.% H$_2$O
Water content (wt.%)
0.0
1.0
2.0
3.0
4.0
5.0
6.0
700
800
900
1000
1100
Temperature (°C)
(b)
Water content (wt.%)
0.2
0.4
0.6
0.8
1.0
Melt fraction
(c)
Silica content (wt.%)
66
68
70
72
74
76
78
Temperature (°C)
(d)
Water content (wt.%)
Silica content (wt.%)

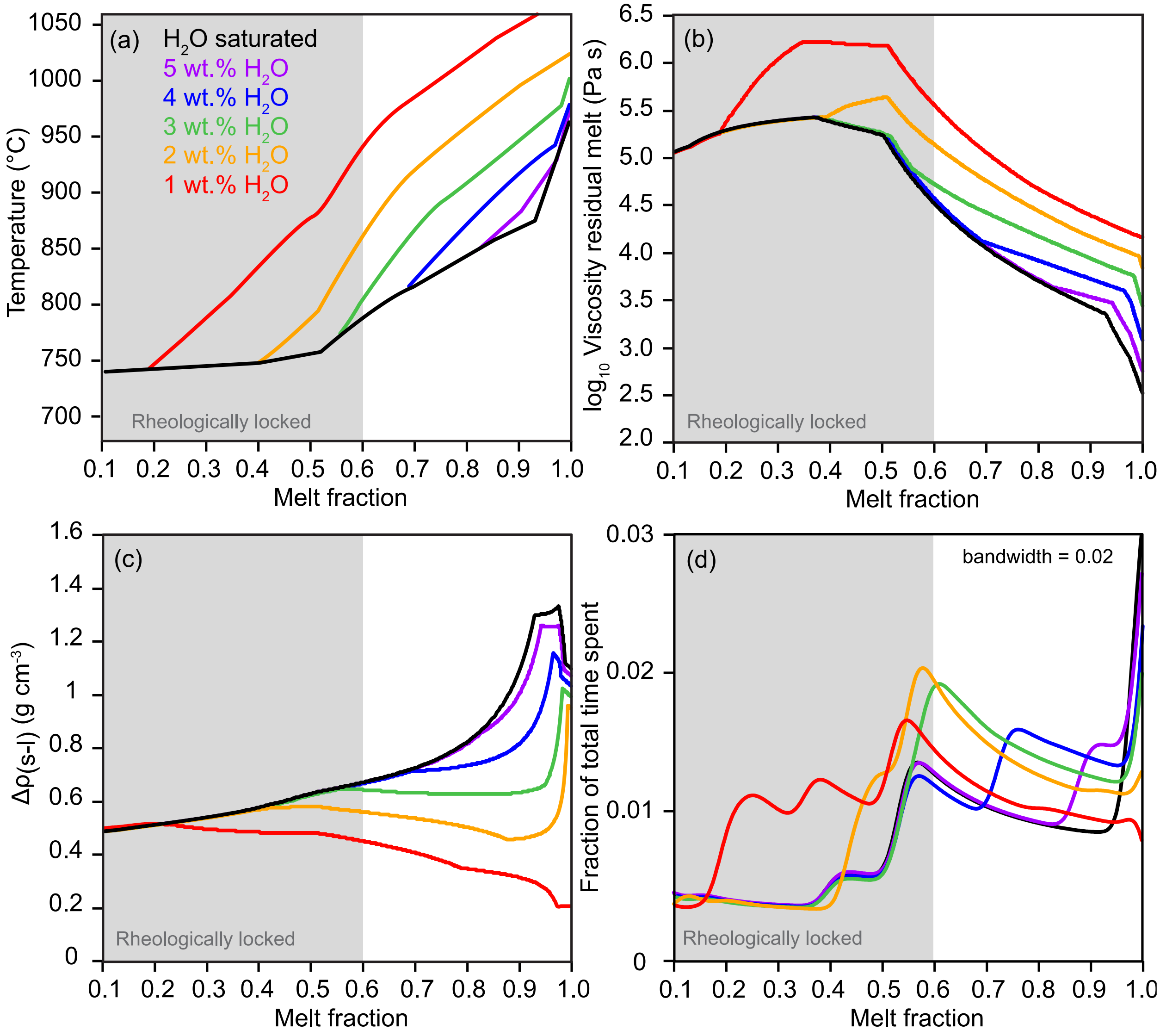
(a)
H_2O saturated
5 wt.% H_2O
4 wt.% H_2O
3 wt.% H_2O
2 wt.% H_2O
1 wt.% H_2O
Temperature (°C)
1050
1000
950
900
850
800
750
700
Rheologically locked
0.1 0.2 0.3 0.4 0.5 0.6 0.7 0.8 0.9 1.0
Melt fraction
(b)
$\log_{10}$ Viscosity residual melt (Pa s)
6.5
6.0
5.5
5.0
4.5
4.0
3.5
3.0
2.5
2.0
Rheologically locked
0.1 0.2 0.3 0.4 0.5 0.6 0.7 0.8 0.9 1.0
Melt fraction
(c)
Δρ(s-l) (g cm^{-3})
1.6
1.4
1.2
1
0.8
0.6
0.4
0.2
0
Rheologically locked
0.1 0.2 0.3 0.4 0.5 0.6 0.7 0.8 0.9 1.0
Melt fraction
(d)
bandwidth = 0.02
Fraction of total time spent
0.03
0.02
0.01
0
Rheologically locked
0.1 0.2 0.3 0.4 0.5 0.6 0.7 0.8 0.9 1.0
Melt fraction

806

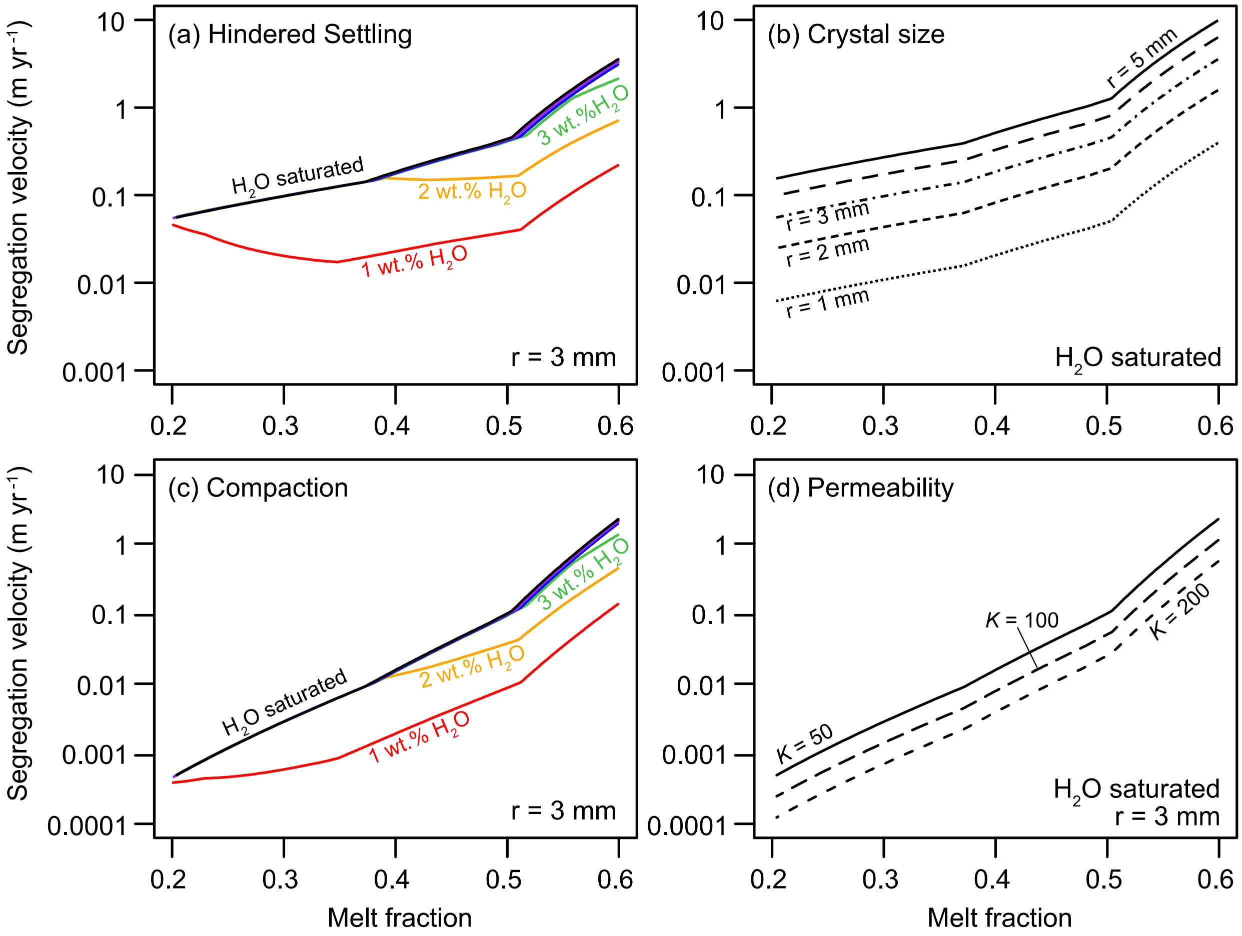

(a) Hindered Settling
(b) Crystal size
(c) Compaction
(d) Permeability
Segregation velocity (m yr^{-1})
Melt fraction
10
1
0.1
0.01
0.001
0.0001
0.2
0.3
0.4
0.5
0.6
H_2O saturated
3 wt.%H_2O
2 wt.% H_2O
1 wt.% H_2O
r = 3 mm
r = 5 mm
r = 2 mm
r = 1 mm
K = 50
K = 100
K = 200

807

808

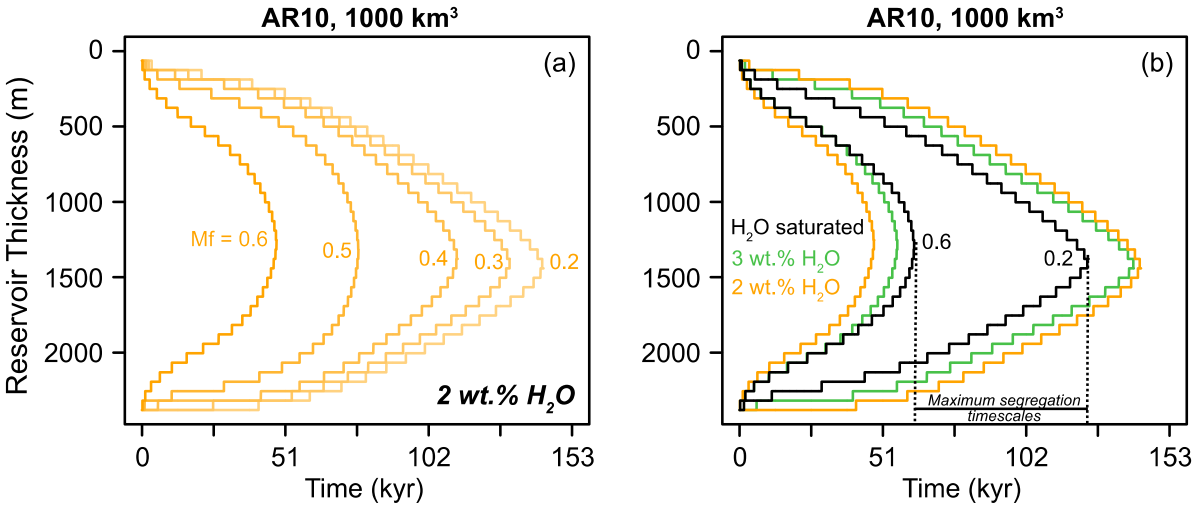
AR10, 1000 km³
(a)
Reservoir Thickness (m)
0
500
1000
1500
2000
Mf = 0.6
0.5
0.4
0.3
0.2
2 wt.% H₂O
0
51
102
153
Time (kyr)
AR10, 1000 km³
(b)
H₂O saturated
3 wt.% H₂O
2 wt.% H₂O
0.6
0.2
Maximum segregation timescales
0
51
102
153
Time (kyr)

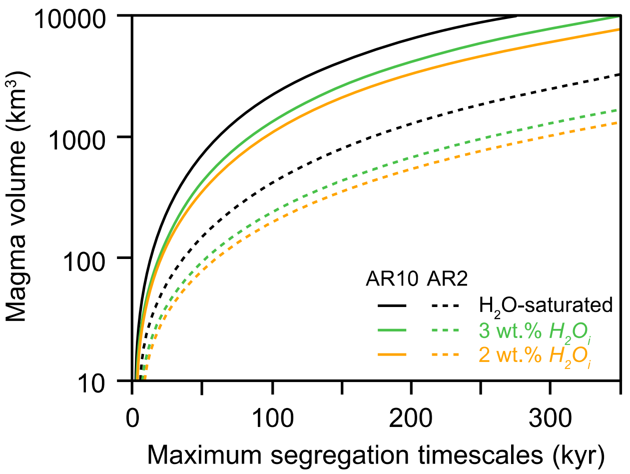
10000
1000
100
10
Magma volume (km³)
0
100
200
300
Maximum segregation timescales (kyr)
AR10 AR2
H₂O-saturated
3 wt.% H₂Oᵢ
2 wt.% H₂Oᵢ

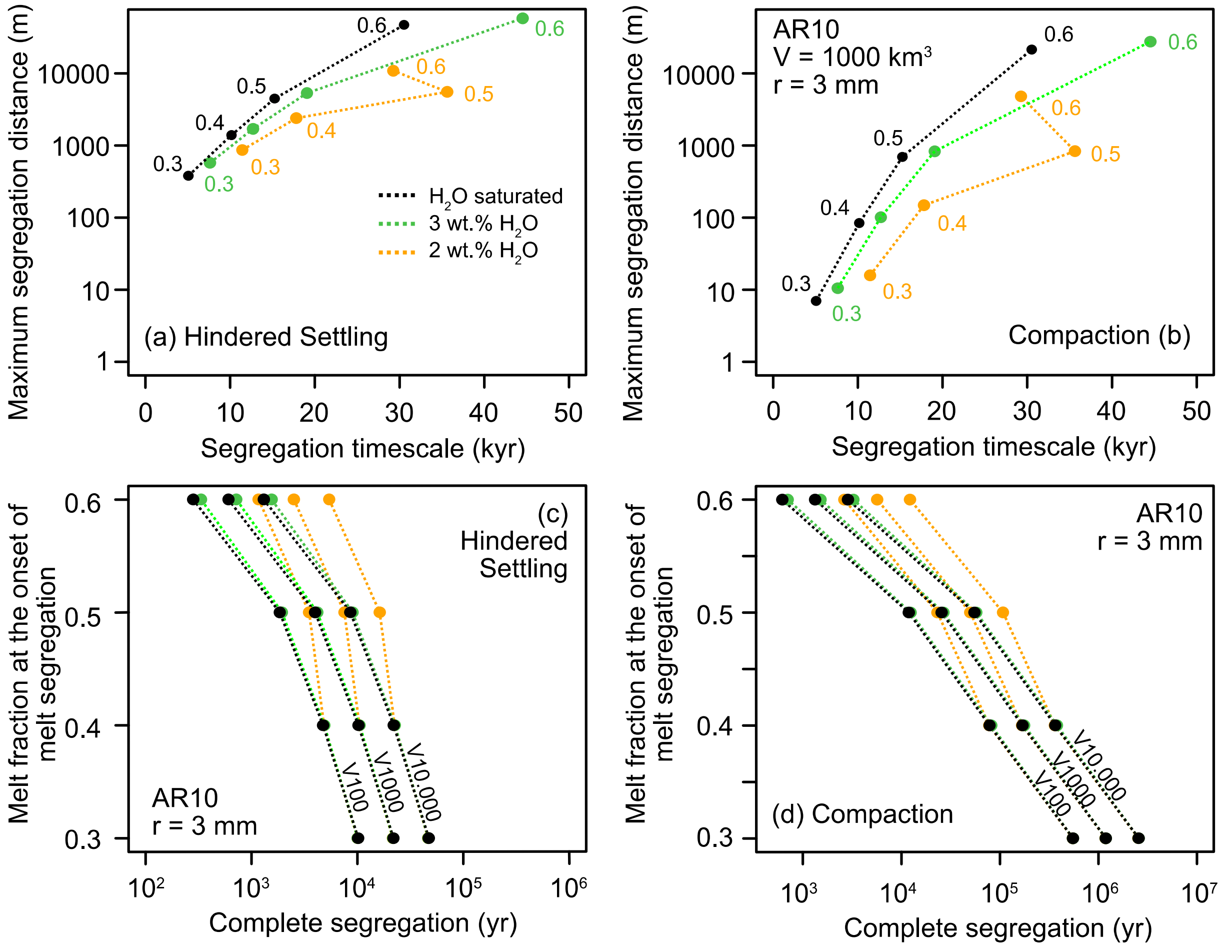

Maximum segregation distance (m)
10000
1000
100
10
1
0.6
0.5
0.4
0.3
H2O saturated
3 wt.% H2O
2 wt.% H2O
(a) Hindered Settling
0
10
20
30
40
50
Segregation timescale (kyr)
AR10
V = 1000 km³
r = 3 mm
Compaction (b)
Melt fraction at the onset of melt segregation
(c) Hindered Settling
AR10
r = 3 mm
V100
V1000
V10,000
10²
10³
10⁴
10⁵
10⁶
Complete segregation (yr)
(d) Compaction
10⁷

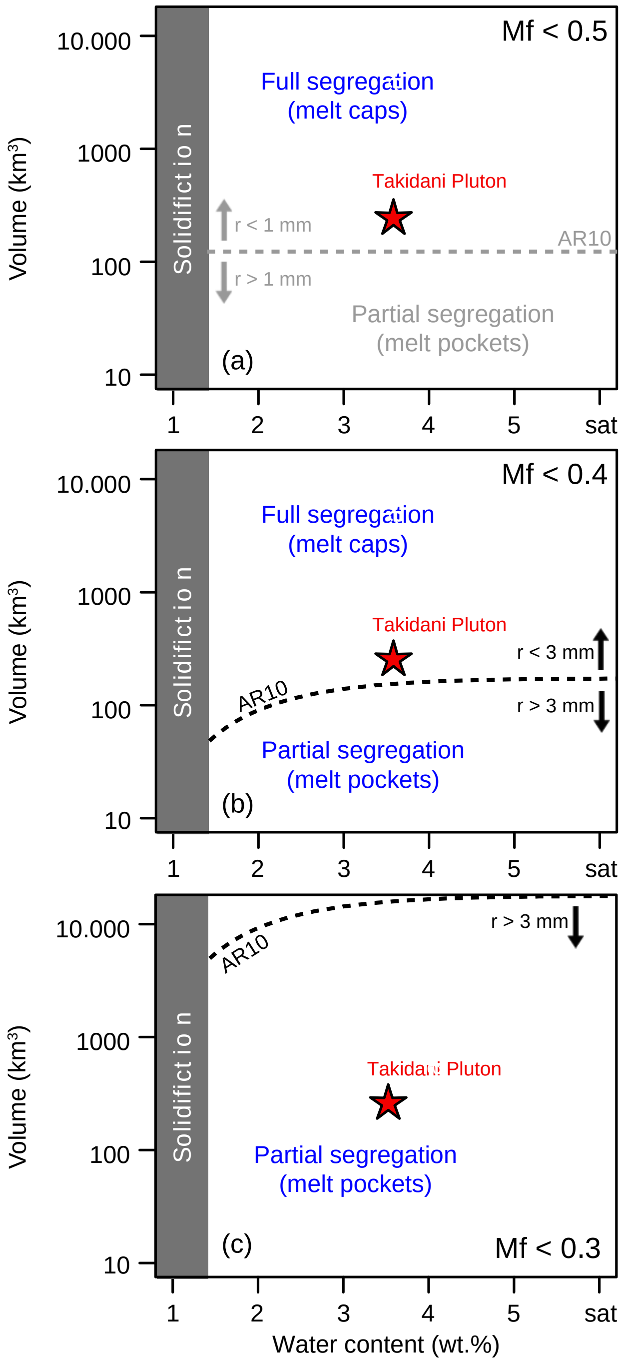
Mf < 0.5
Full segregation
(melt caps)
Takidani Pluton
r < 1 mm
AR10
r > 1 mm
Partial segregation
(melt pockets)
(a)
Mf < 0.4
Full segregation
(melt caps)
Takidani Pluton
r < 3 mm
AR10
r > 3 mm
Partial segregation
(melt pockets)
(b)
AR10
r > 3 mm
Takidani Pluton
Partial segregation
(melt pockets)
(c)
Mf < 0.3
Solidification
Volume (km³)
10.000
1000
100
10
1
2
3
4
5
sat
Water content (wt.%)